Energy & Environmental Science

ROYAL SOCIETY OF CHEMISTRY

COMMUNICATION

View Article Online
View Journal | View Issue

Cite this: *Energy Environ. Sci.*, 2025, **18**, 602

Received 22nd August 2024,
Accepted 4th November 2024

DOI: 10.1039/d4ee03789h

rsc.li/ees

Dislocation-engineered piezocatalytic water splitting in single-crystal $BaTiO_3$†

Yan Zhang,[a] Kaiyu Feng,[a] Miao Song,*[a] Shan Xiang,[a] Yan Zhao,[a] Hanyu Gong,[a] Fan Ni,[b] Felix Dietrich,[c] Lovro Fulanović,[b] Fangping Zhuo,*[b] Gerd Buntkowsky,[c] Till Frömling,[bd] Dou Zhang,*[a] Chris Bowen[e] and Jürgen Rödel[b]

The rapid development of society has exacerbated energy scarcity, making water splitting a promising solution for humanity to produce green hydrogen. Therefore, enhancing the relatively low catalytic performance of piezoelectric bulk catalysts is crucial to unlocking their potential for broader practical applications and potentially alleviating contemporary energy demands. Here, we introduce a sustainable doping strategy that deliberately imprints dislocations and their associated strain fields without additional elements into barium titanate single crystals to address the challenges faced by bulk piezoelectric catalysts. The presence of highly-oriented {100}⟨100⟩ dislocations in plastically deformed materials was observed utilizing bright-field transmission electron microscopy. The strains induced by dislocations were mapped using high-angle annular dark-field and geometric phase analysis techniques. According to experimental observations and density functional theory calculations, the deformed materials exhibit superior performance in terms of electrical conductivity, ultrasonic response, and hydrogen adsorption-free energy. As result a nearly fivefold increase in piezoelectric catalytic performance, as compared to undeformed reference materials, is achieved. Our work demonstrates the potential of dislocation engineering to boost bulk piezoelectric catalysts, thereby challenging the current reliance on powder-based catalysts.

Broader context

The potential of piezoelectric materials to utilize mechanical energy for water splitting and hydrogen production offers a new approach to addressing the energy crisis. While bulk piezocatalysts have high application potential due to their ability to be easily retrieved and reused, the need to improve the hydrogen production efficiency of bulk materials remains a significant challenge. To address this issue, dislocations and associated strain fields were deliberately introduced into $BaTiO_3$ single crystals at high temperatures to produce high dislocation density materials. The deformed $BaTiO_3$ crystals, with high dislocation density, were shown to exhibit high piezoelectric response currents, increased charge carrier transport capabilities, and an ideal hydrogen adsorption free energy, thereby significantly enhancing their water splitting efficiency for hydrogen production. On conducting piezocatalytic experiments over multiple cycles, the deformed $BaTiO_3$ crystals continued to demonstrate stable water splitting and hydrogen production capabilities. This novel form of retrievable and stable piezocatalyst has significant potential to open new avenues in the field of water splitting for hydrogen production.

1. Introduction

The extraction and use of fossil fuels, including petroleum, coal, and natural gas, have led to energy shortages and significant environmental pollution, which is exacerbating global warming.[1] As a result, hydrogen is attracting increasing interest as a versatile, clean, and sustainable energy source with a high energy density, which is beneficial to sustainable development.[2–4] In recent years, photo-catalysis[5] and electrocatalysis[6] have been extensively reported with regard to hydrogen production by water splitting. However, photo-catalysis is limited due to its dependence on a light source.[7] In addition, while electrocatalysis possesses a high efficiency for hydrogen production, the consumption of electrical energy significantly increases its costs.[8] Compared to these methods, piezocatalysis offers a stable and low-cost alternative for water splitting by converting mechanical vibrations such as sound waves, wind, and water flow into useful electric energy.[9–11] The approach has already demonstrated that multiple reactions can be catalyzed or induced by the generation of a large piezopotential, including water splitting, organic reactions (including polymerization), sterilization, dye degradation, and even tumor destruction.[9] Point-defect engineering is a prevalent method for enhancing hydrogen production using powder-based catalysts, however, the use of the catalytic material in powder form poses

[a] State Key Laboratory of Powder Metallurgy, Central South University, Changsha, Hunan 410083, China. E-mail: songmiao@csu.edu.cn, dzhang@csu.edu.cn
[b] Department of Materials and Earth Sciences, Technical University of Darmstadt, 64287 Darmstadt, Germany. E-mail: zhuo@ceramics.tu-darmstadt.de
[c] Institute of Physical Chemistry, Technical University of Darmstadt, 64287 Darmstadt, Germany
[d] Fraunhofer IWKS, Fraunhofer Research Institution for Materials Recycling and Resource Strategies, Hanau, Germany
[e] Department of Mechanical Engineering, University of Bath, Bath BA2 7AY, UK

† Electronic supplementary information (ESI) available. See DOI: https://doi.org/10.1039/d4ee03789h

challenges, such as difficulties in retrieval and reuse, potentially leading to secondary water pollution. This issue currently limits the practical application of piezoelectric materials in hydrogen production. The use of catalysts in bulk form, which can be readily retrieved for reuse, could address this problem and achieve effective H_2 production.[12] Nevertheless, beyond chemical doping, boosting the catalytic performance of piezoelectric bulk catalysts remains a formidable challenge since conventional wisdom suggests that powder-based materials, with their higher specific surface area and more active sites, are more effective for catalytic reactions.

Piezocatalysis essentially means exploiting a piezoelectric or ferroelectric polarization to induce reactions at the surface of a material.[13,14] While the underlying mechanism remains elusive, two mechanisms are hypothesized concerning redox reactions, namely the energy band theory and the screening charge effect.[13] Band theory explains the regulation of the band structure by the piezoelectric effect and the control of the flow direction of internal charge carriers, thereby allowing the reaction to occur. The screening charge effect describes the piezopotential induced directly at the material's surface. Internal and external charges will eventually lead to a screening of the respective potential. However, in a short time frame, the potential at the surface can be sufficiently high to induce a redox reaction if it is higher than the respective Gibb's free activation enthalpy of the reaction. Eventually, internal and external charge carriers will lead to a screening of the piezoelectrically induced potential for both mechanisms discussed. Therefore, an alternating mechanical excitation is required for chemical reactions to continue. A piezopotential may, nevertheless, also catalyze further surface reactions that do not involve electron transfer from, or to, the materials' surface.[15–19] The change in potential or electric field, respectively, may be sufficient to modify reactions close to, or at, the surface.

Multiple approaches have been discussed in the literature to elevate the yield from piezocatalysis. These can be classified as modifications of the bulk semiconducting behavior, surface properties, and the piezoelectric properties of the ceramic.[20] Furthermore, the synthesis of heterojunctions between semiconductors and decorations using an additional metallic catalyst can be employed.[21,22] In the case of bulk semiconducting behavior, doping of materials such as lead zirconate titanate (PZT) can result in a narrower band gap to enhance the piezocatalytic efficiency.[23] Regarding surface modification, surface defects, such as oxygen vacancies, can act as catalytically active sites. Zheng *et al.* analyzed the impact of strain and sulfur vacancies on the hydrogen production rate using MoS_2 powders, demonstrating that optimal performance can be achieved through the synergistic combination of a certain degree of strain and sulfur vacancies.[24] There is general agreement that the achievable piezopotential is the single most important factor.[20] Therefore, recent studies have heavily focused on ferroelectric materials because of the vast opportunities to extensively modify their piezoelectric properties.[25] Nevertheless, chemical methods such as doping and the creation of morphotropic phase boundaries are common techniques used to enhance the piezoelectric potential in ferroelectric solid solutions, which have been shown to increase the catalytic efficiency of poled samples.[26]

In functional oxides, one-dimensional (1D) dislocations carry both a strain field and a local charge with a compensating envelope, thereby self-assembling into larger-scale structures such as networks that span dimensions of nanometers to millimeters. Due to the intrinsically strong coupling between lattice strains and polarization charges, the introduction of charged dislocations and their associated strains into ferroelectrics has gained significant interest in tuning functionality.[27–29] For example, extraordinary piezoelectric coefficients (>2000 pm V^{-1}) can be obtained in single-crystal $BaTiO_3$, where 1D dislocations interact with two-dimensional domain walls, acting as sites for domain nucleation and pinning centers for domain wall motion. Interestingly, dislocations serve as scattering centers for elementary particles such as phonons and electrons, making them a powerful tool for tailoring the electronic, thermal, and optical properties such as apparent band gap and electrical conductivity.[30–33] The formation of dislocation networks creates innumerable active sites for surface reactions (*e.g.*, generation of hydroxyl radicals) and conductive pathways, and the resulting changes in surface potential[34,35] offer a new proof of concept to enhance bulk catalyst efficiency. It has been hypothesized that dislocations in the in-plane and out-of-plane directions of MoS_2 nanosheets can enhance water splitting.[36] However, the density of dislocations introduced by this method and their effects on the catalytic process remain rather undefined.

In this work, we use classical ferroelectric $BaTiO_3$ as a model system to study the effects of plastic deformation on electrical and piezocatalytic properties. Numerous dislocations oriented along the [001] crystallographic direction were successfully introduced into $BaTiO_3$ single crystals through high-temperature plastic deformation, producing deformed samples with different types of exposed dislocations on the crystal faces after mechanical cutting. The deformed samples exhibit improved carrier mobility, ultrasonic excited response, and hydrogen adsorption-free energy, thus significantly enhancing the piezocatalytic hydrogen production performance. Our results demonstrate the potential of plastic deformation and dislocation engineering to achieve improved hydrogen production in bulk piezoelectric catalysts, potentially addressing issues inherent in traditional hydrogen production methods.

2. Results and discussion

2.1 Creation of dislocation structures by high-temperature plastic deformation

To introduce a high density of aligned dislocations with $\{100\}\langle100\rangle$ slip systems into $BaTiO_3$ single crystals, we plastically deformed crystals along the [110] direction (Fig. 1a and b) with a force-loading rate of 0.2 N s^{-1} at 1150 °C, see Fig. S1 (ESI†). A well-defined plastic deformation regime can be noted in the stress–strain curve (Fig. S1, ESI†), during which the introduction of directed dislocations into $BaTiO_3$ occurs. The plastic deformation is indicated by a permanent change (approximately 0.26%) in the (200) *d*-spacing, as measured by X-ray diffraction, along with an increase in dislocation density

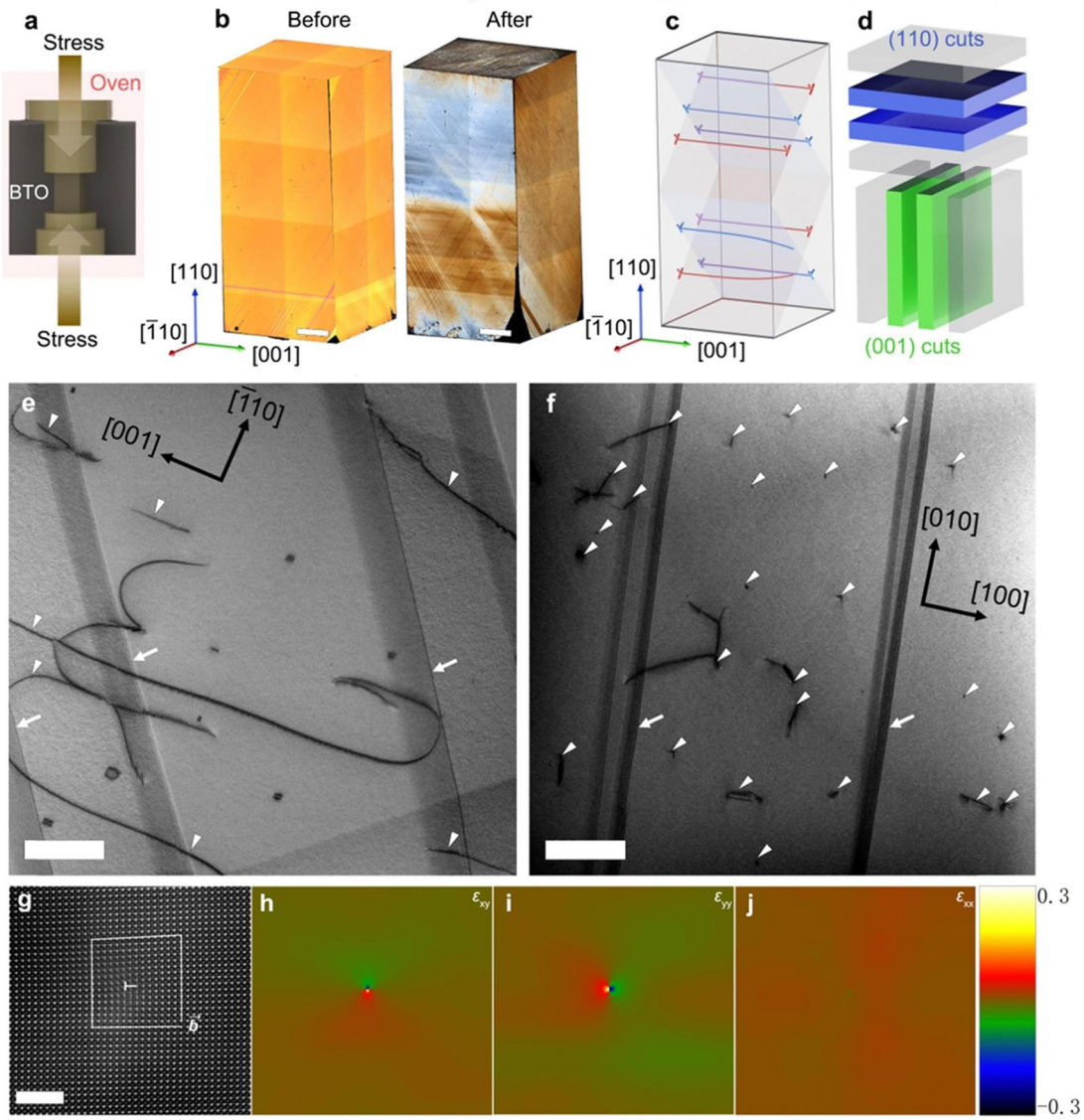

Fig. 1 Creation of dislocation structures by high-temperature plastic deformation. (a) Schematic depicting the alignment of a $BaTiO_3$ single crystal under uniaxial compression. (b) Typical domain arrangement for a tetragonal [110]-oriented $BaTiO_3$ single crystal imaged with differential interference contrast before and after deformation. Scale bar: 1 mm. (c) Schematic of the high-temperature {100}⟨100⟩ slip systems activated during uniaxial compressive plastic deformation. (d) Schematic represents the sample slicing. Bright-field TEM images of dislocations forming in deformed $BaTiO_3$ crystal when viewed on (e) (110) plane, and (f) (001) plane. White arrowheads and arrows indicate the positions of dislocations and domain walls, respectively. Scale bars are 500 nm. (g) HAADF image of the dislocation core of a [100]-type dislocation with Burgers circuit. Scale bar is 5 nm. Experimental strain fields: (h) ε_{xy}, (i) ε_{yy}, and (j) ε_{xx}.

by three to four orders of magnitude.[37] The mechanical imprint is macroscopically reflected in the altered domain structure, see Fig. 1b. To understand the effect of imprinted dislocations on the domain structure, we have performed angle-dependent ^{137}Ba solid-state nuclear magnetic resonance (NMR) spectra (Fig. S2, ESI†) and then calculated the relative amounts of individual domain configurations from them (Fig. S3 and S4, ESI†). Note that *a*-domains feature spontaneous polarization vectors that are parallel to the [100] (namely, a_1-domains) and [010] (namely, a_2-domains) directions, whereas *c*-domains display polarization vectors along the [001] direction. The macroscopic manifestation of our mechanical dislocation imprint is evident through the altered *c*/*a* domain ratios from 38% (reference sample) to 79% (deformed sample), as highlighted in Fig. S4 (ESI†).

In order to describe the character of the imprinted dislocations, transmission electron microscopy (TEM) images were taken after preparing samples by cutting the deformed crystal into pieces parallel to the (110) and (001) planes (Fig. 1d). Traces of dislocation lines (marked by white arrowheads) are likely to run along the [001] direction (see Fig. 1e), featuring dislocation points (pure edge dislocations) and short dislocation segments on viewing the dislocations along the [001] direction; see Fig. 1e. These short segments may originate from the screw part of the mixed dislocations.[29] The dislocation

density is estimated to be 1.5×10^{12} m^{-2}, corresponding to an average dislocation spacing of 815 nm (Fig. S5, ESI†). The orientation of the sliced samples was verified from the Fast Fourier transform (FFT) pattern, see Fig. S6 (ESI†). Fig. 1g highlights a typical high-angle annular dark-field (HAADF) image of a dislocation core, acquired along the [001] zone axis for the deformed sample, confirming a Burgers vector of [100]/2. This is determined by the geometrical phase analysis (GPA) of the HRTEM image, which reveals a strain singularity (ε_{xy}, ε_{yy}, and ε_{xx}) around the dislocation core; see Fig. 1h–j.

2.2 Exposing dislocations on surfaces and conductivity

Despite the high density of dislocations in deformed samples, the interior of the ferroelectric material cannot directly participate in catalysis. Therefore, for piezocatalytic experiments, cutting of the deformed samples to fully expose the imprinted dislocations is necessary.

As indicated in Fig. 2a, dislocations are present on the surface of the deformed sample after cutting along the (001) crystal plane (hereafter named (001)-cut), featuring dislocation points. Fig. 2b illustrates the cutting process along the (110) crystal plane (named (110)-cut), where dislocations on the surface appear as dislocation lines parallel to the surface. Dislocations and their associated strains in deformed samples may significantly promote the piezoelectric catalytic process,[24,36] as the local strain field near the dislocation core can reach several GPa.[38] Note that the (001)-cut sample provided in Fig. 2a has a larger area with fully exposed dislocation points as compared to the (110)-cut sample highlighted in Fig. 2b. Specifically, the (001)-cut samples have an exposure area of $\sim 4 \times 4 \times 2$ mm^2, resulting in 4.8×10^7 dislocation cores, while the (110)-cut samples have an exposure area of $\sim 4 \times 1 \times 2$ mm^2, accounting for 1.2×10^7 dislocation cores. The high number of dislocations creates many potential active centers for piezocatalysis.

As the introduced dislocations carry both a strain field and a local charge, we quantified the electrical conductivity of the reference and deformed samples at room temperature. As shown in Fig. S7 (ESI†), the conductivity of the deformed samples from both cuts reveals a significant increase, indicating enhanced carrier mobility and more efficient charge transport.[39] Fig. 2c highlights the electrochemical impedance spectroscopy (EIS) Nyquist plots of the deformed samples and reference samples. The smaller arc radii of the deformed samples indicate a relatively lower resistance,[40] demonstrating that their interface charge transfer resistance is lower and carrier transport is improved. In addition, when subject to ultrasound, the deformed samples exhibit a higher piezo-current density, revealing a greater ultrasonic excited response (see Fig. 2d).

2.3 Potential distribution of $BaTiO_3$ single crystals at different ultrasonic frequencies

To predict the piezoelectric potential distribution of $BaTiO_3$ single crystals under varying ultrasonic frequencies, finite element modeling (FEM) was employed. This method meticulously follows the equations provided in the Experimental section and replicates the actual dimensions of the $BaTiO_3$ crystals in terms of length, width, and height.

Previous research[41] suggests that the stress induced by the collapse of cavitation bubbles during ultrasound exposure is inversely proportional to the square of the frequency (f). Fig. 3 illustrates the dynamic potential distribution in $BaTiO_3$ single crystals at different ultrasonic frequencies, highlighting the response of their piezoelectric properties to acoustic stimulation. At a frequency of 45 kHz, there is an apparent increase in the fluctuation of the piezo-potential (Fig. 3a–e), which signifies an enhanced piezoelectric activity. This enhancement is particularly evident in the progression from lower to higher generated voltages. In contrast, at higher frequencies of 80 kHz and 100 kHz, as shown in the middle and bottom rows (Fig. 3f–j and k–o), the potential variation across the cycle is minimal, indicating a stable, yet low, piezoelectric response, which is further detailed by the complex potential and stress distribution patterns at mid-cycle points (Fig. S8 and S9, ESI†).

The analysis of piezoelectric potentials at different time intervals, corresponding to the varying frequencies of applied stress, reveals that the highest piezoelectric potential occurs at a frequency of 45 kHz, surpassing those observed at 80 kHz and 100 kHz. Given that higher ultrasound frequencies result in more cycles within the same time period, further research is warranted to quantify the piezoelectric charge generated during these intervals to better assess the catalytic performance of $BaTiO_3$ under different conditions. Fig. 3p–r, illustrating the amount of piezoelectric charge generation at frequencies of 45 kHz, 80 kHz, and 100 kHz within the same time frame, reveals that higher frequencies do not always result in greater charge generation, as indicated by the integration of the curves with the horizontal axis ($Q_1 > Q_2 > Q_3$).

2.4 Piezoelectric catalytic hydrogen production rates and DFT calculation

Fig. 4a and b present a comparison of piezocatalytic hydrogen production across various ultrasound frequencies. The results demonstrate that at a lower ultrasonic frequency of 45 kHz, the piezoelectric catalytic hydrogen production rate is the highest for both the deformed samples and reference samples, surpassing those observed at 80 kHz and 100 kHz. This phenomenon is due to cavitation bubbles growing larger, which enhances cavitation effects and facilitates the generation of a greater quantity of piezoelectric charges within the same duration in $BaTiO_3$ single crystals.[42] These experimental findings are consistent with our FEM results. The hydrogen production rate of the (001)-cut deformed samples at 45 kHz can reach 38.6 mmol h^{-1} m^{-2}, significantly higher than the 11.9 mmol h^{-1} m^{-2} observed in undeformed reference samples. This marked increase highlights the critical role of dislocations in enhancing the piezoelectric catalytic hydrogen production in $BaTiO_3$ single crystals. Similarly, the (110)-cut deformed samples show a hydrogen production rate of 29.1 mmol h^{-1} m^{-2} at an ultrasonic frequency of 45 kHz, which is higher than the reference samples of 9.9 mmol h^{-1} m^{-2}. However, the overall piezoelectric catalytic hydrogen production efficiency of (110)-cut deformed samples is lower than those of (001)-cut samples. This difference aligns with variations in active sites provided by dislocations, conductivity, EIS Nyquist plots, and J–V curves. The single crystals, no matter with or without

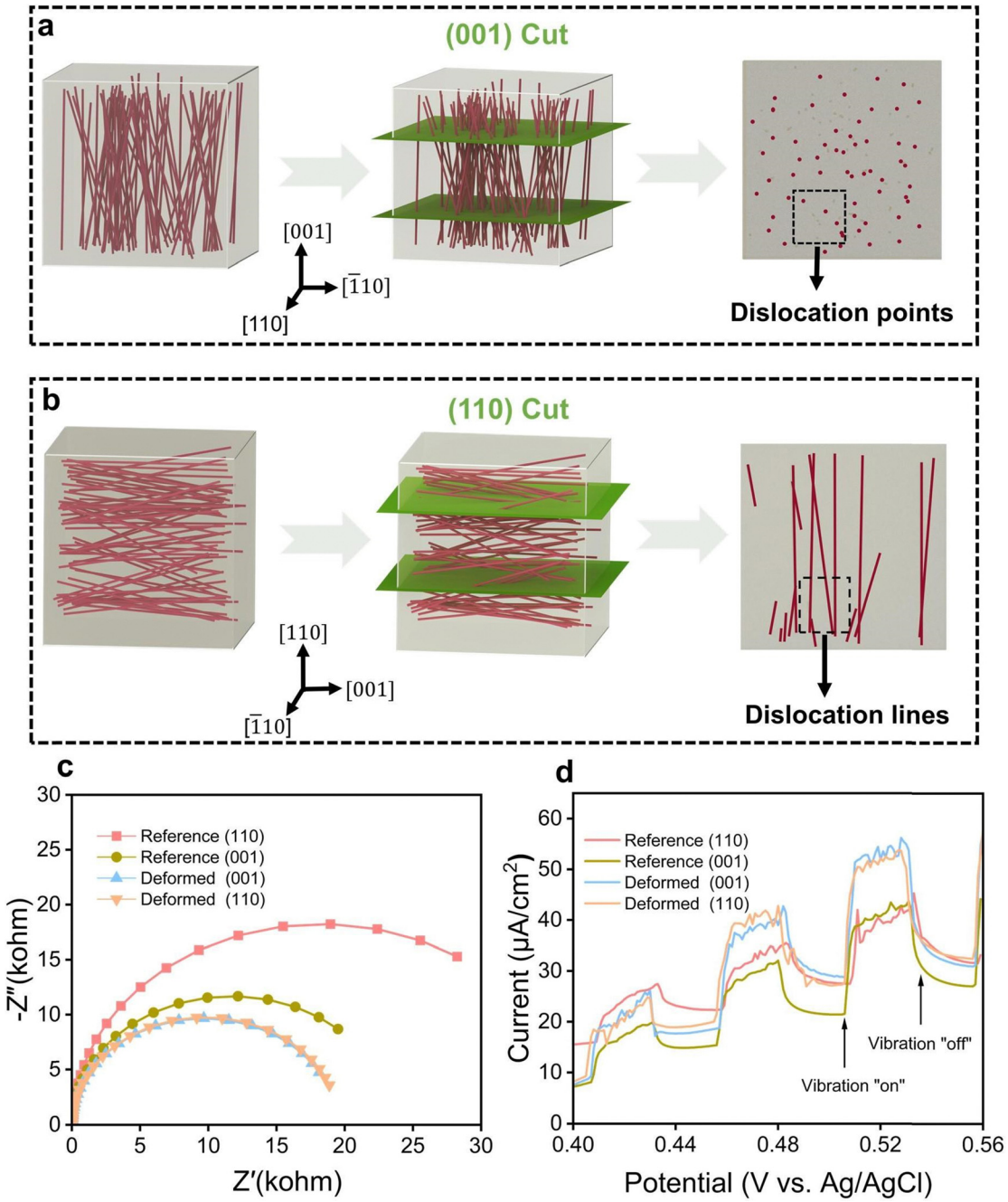

Fig. 2 Exposing dislocations on surfaces and conductivity. Preparation of deformed samples with dislocation points (a) and dislocation lines (b) on the surface. EIS Nyquist plots (c) and piezo-current–potential (*J*–*V*) curve (d) of the deformed and reference samples. The test temperature was room temperature.

deformation, did not exhibit apparent improvement in hydrogen production after poling, compared to the unpoled counterparts; see Fig. S10 (ESI†). Repetitions indicate that all deformed samples exhibit good cyclic stability (Fig. 4c and d). It is also worth noting that when we further increase the dislocation density of the samples up to 1.5×10^{13} m^{-2} by deforming the samples with a notch (see our previous report[37] for detailed determination of the dislocation density), the hydrogen production has correspondingly improved, reaching 53.8 mmol h^{-1} m^{-2} and 40.6 mmol h^{-1} m^{-2} for (001) cut and (110) cut, respectively; see Fig. 4e and f.

Density functional theory (DFT) calculations were employed to determine the effect of the strain induced by dislocations on the level of piezocatalytic hydrogen produced. The strain induced by the existence of dislocations can lead to lattice distortion.[38] Based on TEM and geometrical phase analysis results[38] (Fig. 1) and the measured lattice constants (Fig. S6, ESI†), an average tensile strain of 2–3% was observed within approximately 1.5 nm of the dislocation core on the side opposite to the extra half-plane of atoms. Models of $BaTiO_3$ with 0%, 2%, and 3% tensile strain, including cuts along the (001) and (100) crystal planes, were established according to the observed strain; see Fig. S11–S15 (ESI†). The

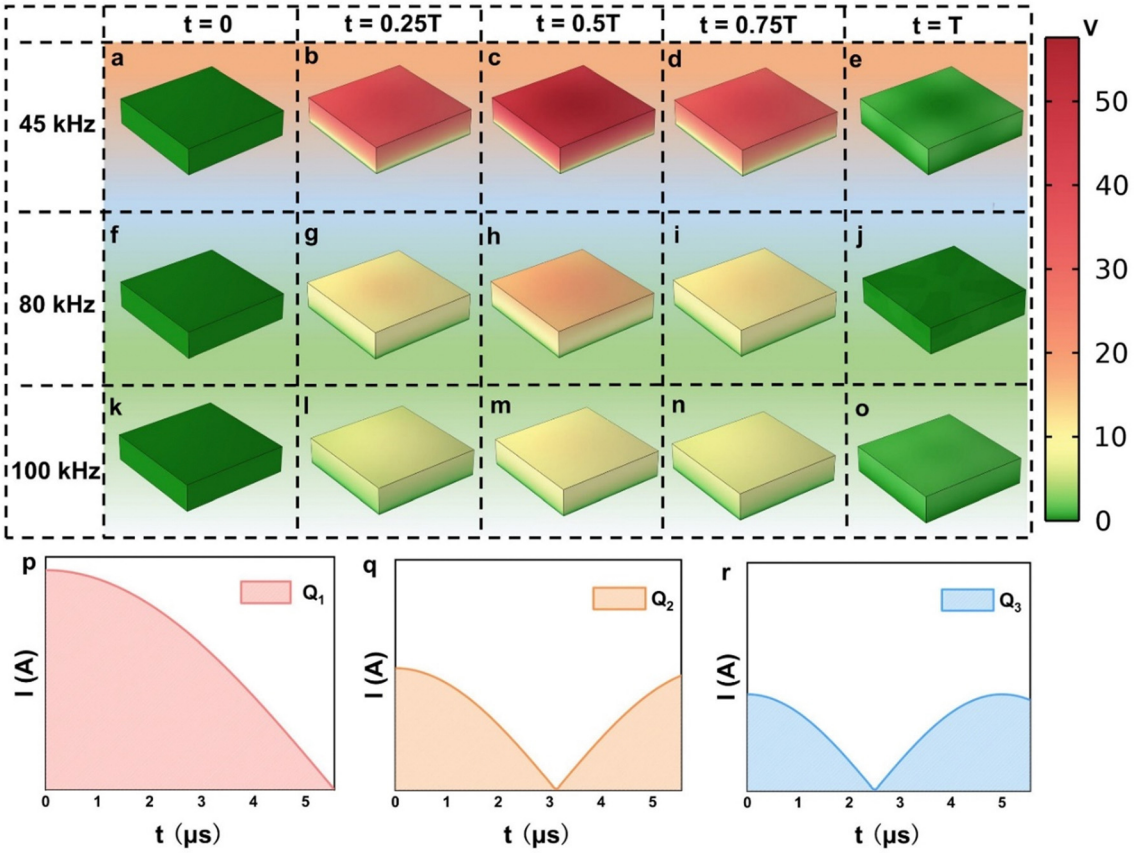

Fig. 3 Potential distribution of $BaTiO_3$ single crystals with different ultrasonic frequencies. The instantaneous potential distribution at t = 0 (a), t = 0.25 T (b), t = 0.5 T (c), t = 0.75 T (d), and t = T (e) with the ultrasonic frequency of 45 kHz. Note that T is the period of the ultrasound waves, which is the reciprocal of frequency (f). The instantaneous potential distribution at t = 0 (f), t = 0.25 T (g), t = 0.5 T (h), t = 0.75 T (i), and t = T (j) with an ultrasonic frequency of 80 kHz. Instantaneous potential distribution at t = 0 (k), t = 0.25 T (l), t = 0.5 T (m), t = 0.75 T (n), and t = T (o) with an ultrasonic frequency of 100 kHz. Periodic model for the amount of charge generated by the piezoelectric potential at an ultrasonic frequency of 45 kHz (p), 80 kHz (q), and 100 kHz (r).

hydrogen adsorption Gibbs free energy (ΔG_H) of all models were investigated as depicted in Fig. 4g, h and Tables S1 and S2 (ESI†). The most ideal value for ΔG_H is 0, where the surface binding with hydrogen is neither too weak nor too strong,[24,43] which is most conducive to hydrogen production. Fig. 4g indicates that a 2% strain can significantly improve the ΔG_H of [001]-oriented $BaTiO_3$. However, further amplification of strain may not necessarily be more advantageous for ΔG_H, and when the strain is increased to 3% there is no further improvement in ΔG_H; and a slight deterioration in ΔG_H is observed. Fig. 4h reveals that strain also has a beneficial effect on ΔG_H of the [110]-oriented sample, although this effect is significantly smaller than that observed for the [001] orientation. In addition, the effect of a 2% strain on ΔG_H is also more pronounced than that of a 3% strain. Therefore, the significant enhancement in piezoelectric catalytic hydrogen production of deformed samples is attributed to the combined effects of improved piezoelectric charge coefficient, a ΔG_H which is closer to 0, and the accumulation and transfer of charge near dislocations.[36] The piezocatalytic mechanism of the deformed and reference samples is illustrated in Fig. 4i–p. As featured in Fig. 4i and m, balanced binding charges and screening charges render the material electrically neutral. However, due to lattice distortions in the deformed sample, a larger electric potential is generated.[44,45] A subsequent application of compressive stress causes the amplitude of polarization to decrease (Fig. 4j and n), leading to the release of screening charges from the surface until a new equilibrium is reached. The deformed sample can release more charges in the process for the following reasons.[46] The relationship between the stress applied to a piezoelectric material and the resulting electric charge can be described in eqn (1), and there is a proportional relationship between stress and strain as indicated in eqn (2). We assume that eqn (2) is applicable to the entire sample, including the dislocation core. Therefore, the stress concentration induced by dislocations will result in a greater strain, and the strain can contribute more charge and a higher current according to eqn (3). These observations are consistent with the results observed in the J–V curves displayed in Fig. 2d.

$$\mathrm{d}Q = d_{33} \times \mathrm{d}F = d_{33} \times A \times \mathrm{d}\sigma \quad (1)$$

$$\sigma = E\varepsilon \quad (2)$$

$$I = \frac{\mathrm{d}Q}{\mathrm{d}t} = d_{33} \times \frac{\mathrm{d}F}{\mathrm{d}t} = d_{33} \times A\frac{\mathrm{d}\sigma}{\mathrm{d}t} = d_{33} \times EA\frac{\mathrm{d}\varepsilon}{\mathrm{d}t} \quad (3)$$

where I, Q, σ, ε, A, E and t represent the piezoelectric current, charge, applied stress, strain, surface area, elastic modulus and time, respectively.

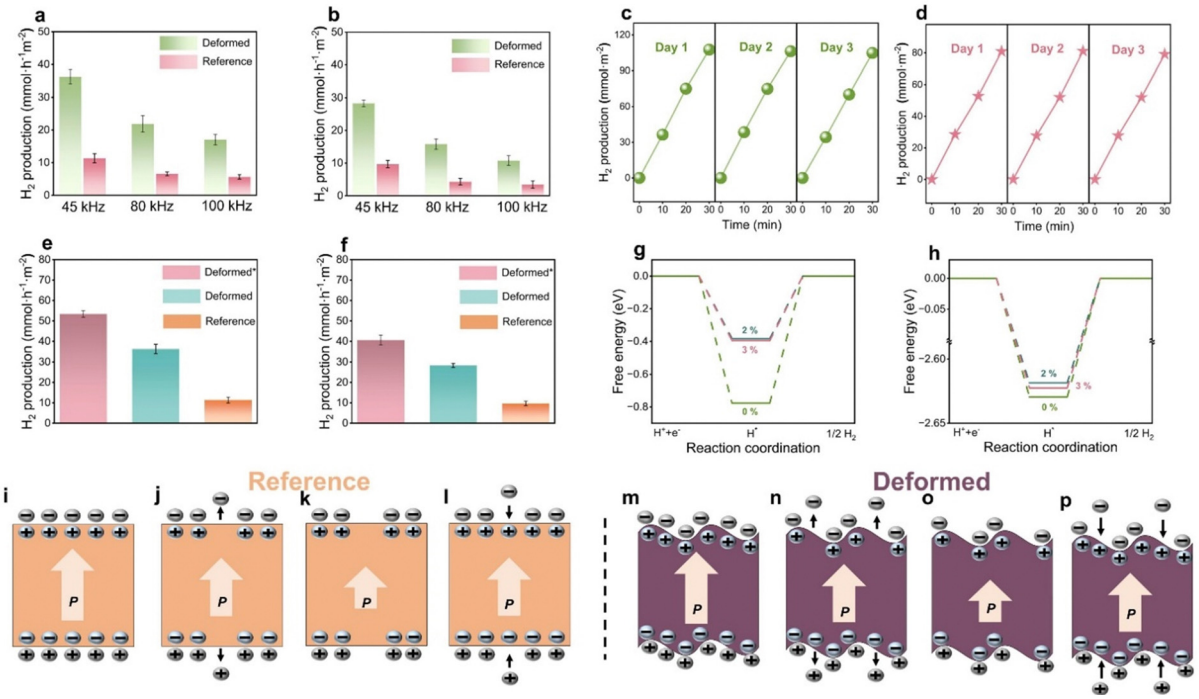

Fig. 4 Piezoelectric catalytic hydrogen production rates and DFT calculation. Piezoelectric catalytic hydrogen production rates of deformed samples and reference samples (a) (001) cut and (b) (110) cut, at different ultrasonic frequencies. Hydrogen production cyclic tests for deformed samples (c) (001) cut and (d) (110) cut at an ultrasonic frequency of 45 kHz. Piezocatalytic hydrogen production rates of (001) cuts (e) and (110) cuts (f). The term 'Deformed*' refers to the samples with higher dislocation density of 1.5×10^{13} m^{-2}. Gibbs free energy of the (g) (001), and (h) (110) surfaces of $BaTiO_3$ with different strains. Piezoelectric catalytic mechanism of reference (i)–(l) and deformed (m)–(p) samples based on the screening charge effect.

As mentioned, the mechanism of piezocatalysis has not yet been fully elucidated.[13] In the case of the screening charge model, screening charges are created under mechanical stress until a new equilibrium is reached (see Fig. 4k and o). As the applied pressure decreases, the condition is reversed, causing another change in screening charges. During these equilibration processes, charge transfer can be induced at the surface, triggering redox reactions (Fig. 4l and p). When it comes to the energy band model, the band bending induced by piezoelectric polarization can be so extensive that redox reactions at the interface are favorable. Irrespective of the mechanism, the following conclusions can be made concerning the dislocation impact.

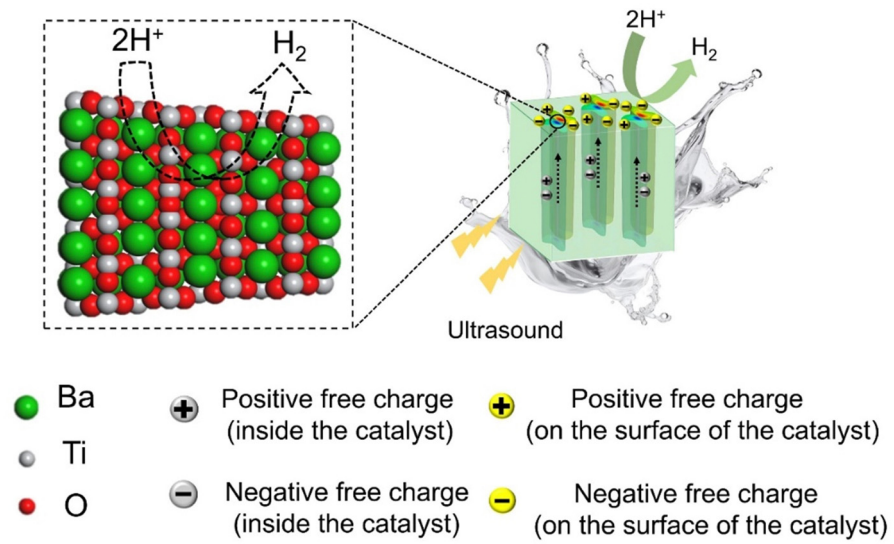

Fig. 5 Illustration of the reaction mechanisms for hydrogen production of the deformed sample under ultrasonic treatment.

The dislocations become catalytically active centers, where a major contribution to this can be attributed to the stress and strain field surrounding the dislocations. The mechanisms of hydrogen production of the deformed sample are illustrated in Fig. 5. The dislocation core causes lattice distortion in the $BaTiO_3$ unit cell, resulting in strain. During the piezocatalytic reaction process, the deformed sample which is experiencing a strain can generate a large number of free charges when subject to ultrasound. The piezoelectric potentials can be developed from two main sources: the separated positive–negative charges and the imprinted charged dislocations. The piezoelectrically-induced and dislocation-trapped positive charges (q^+) can react with water molecules to generate hydrogen (H^+) ions and oxygen products (*e.g.*, hydroxyl radicals or oxygen). Subsequently, these H^+ ions are reduced by negative charges (q^-), leading to the production of H_2. Tens of millions of charged dislocations within the deformed sample afford a facile transfer of charges from the interior of the material to the surface and the negative charges (mainly electrons) can react with H^+ in water. From the perspective of chemical equilibrium of the reaction that produces H_2, the more negative charges transferred by the introduced dislocations, the more favorable it is for the production of H_2. Note that the reference samples exhibit dislocation density ranging from 10^8 to 10^9 m^{-2}. Our mechanical imprinting technique significantly enhances the dislocation density by three to four orders of magnitude. As a result, the presence of a multitude of dislocation sources and their associated local strains can further enhance hydrogen production by adjusting the hydrogen adsorption-free energy, confirmed by our DFT calculations. This opens new avenues for research and potential applications in areas such as piezo-photocatalysts.[47]

3. Conclusions

In summary, defect engineering has been employed to deliberately introduce dislocations into $BaTiO_3$ single crystals *via* high-temperature plastic deformation along the [110] crystallographic direction. Transmission electron microscopy and geometrical phase analysis verified the presence of dislocations, which are characterized by $\{100\}\langle100\rangle$ slip systems with local strains around the dislocations. On stimulation of the ferroelectric surfaces with ultrasonic vibrations, the catalyst converts mechanical energy into electrical energy, facilitating the splitting of water into hydrogen gas. A maximum piezoelectric catalytic hydrogen production efficiency of 53.8 mmol h^{-1} m^{-2} was achieved, which is attributed to a plethora of dislocations and a suited hydrogen adsorption free energy, as compared to undeformed reference samples. Our approach in producing highly active bulk ferroelectric surfaces addresses the challenges of retrieval and reuse faced by powder-based piezoelectric catalysts, thereby advancing the practical application of piezocatalysts. Such interdisciplinary efforts are crucial for advancing our understanding and application of dislocation technology in bulk ferroelectrics, paving the way for innovative solutions in energy and environmental applications and contributing to sustainable technology development.

4. Experimental section

4.1 High-temperature deformation and sample preparation

Top seeded solution grown (TSSG) [110]-oriented high-quality $BaTiO_3$ single crystals with a geometry of $4 \times 4 \times 8$ mm^3 (Electro-Optics Technology GmbH, Idar-Oberstein, Germany) were heated to 1150 °C with a heating rate of 1 °C min^{-1} under a uniaxial compressive stress of 1.25 MPa. To reach thermal equilibrium, temperature and mechanical stress were maintained for 30 min. Then, deformation by uniaxial compression was conducted at 1150 °C using a load-frame (Z010, Zwick/Roell, Ulm, Germany) that was equipped with a linear variable differential transformer (LVDT) for precise measurement of the displacement. A loading rate of 0.2 N s^{-1} and unloading rate of 0.5 N s^{-1} were used to activate the high-temperature slip systems. In this case, the Schmid factor as a quantification for the propensity for dislocation slip on the (100) plane is maximized, which leads to a generation of edge dislocations with a Burgers vector of [100]/2. Afterwards, the sample was cooled down to room temperature at a rate of 1 °C min^{-1} while being subject to a uniaxial compressive stress of 1.25 MPa. Detailed experimental procedures can be found in our previous reports.[27,29,48] To significantly enhance the density of dislocations, the single crystals underwent notching with a diamond wire saw (Well Diamantdrahtsägen GmbH, Germany). This notch, positioned at the center of a (100) plane, penetrated 15–25% of the thickness of the sample. Afterward, these crystals experienced uniaxial compression at 1150 °C, using a Z010 load frame, with compression applied along the [110] axis under identical conditions to those used for unnotched samples. This sophisticated method of mechanical deformation led to a dense, localized network of dislocations.

The deformed crystals were then sliced into smaller pieces perpendicular to the [110] and [001] directions using a Model 4240 Benchtop (Well Diamond Wire Saws, Inc., Norcross, USA). The orientation of the as-prepared samples was confirmed using the Laue back-reflection method (1001 Model, Huber, Rimsting, Germany). The surface of the (001) and (110) cut samples was then polished to a thickness of 0.5–1.0 mm and used in form of plates of lateral dimensions 4 mm and 4 mm. Gold electrodes were sputtered onto two large top and bottom surfaces of the investigated samples, which were then annealed at 200 °C for 2 h (heating/cooling rate: 1 °C min^{-1}) for electrical measurements. Direct current (DC)-poling of both reference and deformed samples was performed under 1 kV mm^{-1} for 10 min at room temperature.

4.2 Dislocation and domain structure characterization

Optical images of the reference and deformed $BaTiO_3$ single crystals were taken using a LEXT OLS4100 laser scanning microscope (Olympus, Shinjuku, Japan). A differential interference contrast (DIC) mode and polarized light mode were used to image domain patterns.

We utilized a low-speed circular saw to slice the samples into 3×3 mm^2 square sheets. Alcohol was employed as a coolant to reduce the temperature and prevent decomposition. The thickness of the specimens was mechanically reduced to 30 μm. Subsequently, an Ar^+ ion beam (GATAN 695) was employed for

final thickness reduction after attaching the specimen to the copper ring (1.5 mm inner diameter). Bright-field TEM images were acquired using an FEI (Thermo Fisher Scientific) TALOS F200X (operating at 200 kV) equipped with a Super-X TEM integrated energy dispersive X-ray spectroscopy system. Another TEM (Spectra 300, Thermo Fisher Scientific, USA) equipped with a high-angle annular dark-field (HAADF) detector was employed at 300 kV for scanning TEM (STEM)-HAADF imaging, with electrons from 59 to 200 mrad collected.

^{137}Ba solid-state NMR spectra were obtained from both deformed and reference single crystals in the unpoled state were collected using a Bruker Avance III HD spectrometer (Bruker, Massachusetts, USA) that was equipped with a wide bore magnet (14.1 T, Oxford). A single-axis goniometer NMR probe (NMR Service, Erfurt, Germany) with nominal resolution of 0.1° was tuned to 66.71 MHz. In this setup, an angle of 0° represents the normal vector of the sample holder that is parallel to the magnetic field B_0. A variety of angles, ranging from 0° to 60°, were selected to measure samples that exposed the (001), (110) and ($\bar{1}$10) faces, respectively. A Hahn-echo sequence with a τ value of 30 μs and a recycle delay time of 1 s was employed, with an acquisition time of 0.05 s. The duration of the 90° pulses was 3.5 μs. A total of 1024 scans were performed, utilizing a sample volume of approximately 4 × 4 × 1 mm^3. The pre-scan delay was set to 10 μs. The chemical shift scale was referenced to a 1 M solution of $BaCl_2$ (0 ppm).

4.3 Electrochemical measurements

The electrical conductivity was quantified by a precision impedance analyser (4294A, Agilent Technologies, Santa Clara, USA). Electrochemical impedance spectroscopy (EIS) and ultrasonic excited piezocurrent–voltage (*J–V*) curves were obtained by a standard three-electrode electrochemical workstation (CHI604E, China) for both deformed and reference specimens. The measurements employed Ag/AgCl electrode (saturated KCl), 0.5 M Na_2SO_4 aqueous solution (pH = 7), and Pt foil as the reference electrode, electrolyte, and counter electrode, respectively. For the EIS investigations, a potential of 0.6 V (*vs.* Ag/AgCl) and an alternating voltage perturbation of 5 mV were applied. *J–V* curves involved cyclic activation of the ultrasonic switch every 5 s, with each ultrasonic stimulation lasting 5 s, and the *J–V* curves were obtained *via* linear sweeping voltammetry at a scan rate of 20 mV s^{-1}.

4.4 Piezoelectric catalysis experiments

15 ml of deionized water was added to a 50 ml reactor, followed by the introduction of a $BaTiO_3$ single crystal into the reactor. The reactor was then placed in a vacuum drying oven and we repeatedly vacuumed the system more than three times at room temperature and evacuated and purged with high-purity nitrogen for 10 min to remove air dissolved in the deionized water. Subsequently, the reactor was transferred to an ultrasonic cleaning device for a hydrogen production by water splitting experiment. The ultrasonic frequency and power were adjusted according to experimental conditions, with a sonication duration of 10 min. The composition of the resulting gas mixture was analyzed using a gas chromatograph (GC-6600, Shanghai Fanwei) that was equipped with a pulsed discharge helium ionization detector (PDHID, VICI, USA).

4.5 Computational details

It has been shown[41] that the stress produced by the collapse of a cavitation bubble during ultrasound, and the strength of ultrasonic effect was related to time interval and volume per unit volume of cavitation bubbles:[49]

$$I_{ca} = \frac{4\pi {R_{max}}^3 P_0}{3T\Delta V} \quad (4)$$

where I_{ca} represents cavitation intensity, R_{max} is maximum instantaneous radius of the bubble, P_0 is air pressure, T is the period of ultrasound waves, which is the reciprocal of frequency (f), and ΔV is a space volume element, respectively. The R_{max} of cavitation bubble can be presented as:[50]

$$R_{max} = \sqrt{3\gamma p_\infty / \rho_L \omega^2} \quad (5)$$

where ρ_L is the mass density of water, p_∞ is the equilibrium of cavitation bubble, γ is the heat capacities ratio, and ω represents angular frequency which is equal to $2\pi f$. Therefore, the relationship between I_{ca} and f can be deduced as:

$$I_{ca} \propto \frac{1}{f^2} \quad (6)$$

We assume the amplitude of the alternating stress applied to $BaTiO_3$ single crystals is proportional to the strength of ultrasonic effect, thus the periodic stress functions can be given in eqn (7)–(9):

$$\sigma_1(t) = A_0 \sin(2\pi f_1 t) \quad (7)$$

$$\sigma_2(t) = A_0 \cdot \left(\frac{f_1}{f_2}\right)^2 \cdot \sin(2\pi f_2 t) \quad (8)$$

$$\sigma_3(t) = A_0 \cdot \left(\frac{f_1}{f_3}\right)^2 \cdot \sin(2\pi f_3 t) \quad (9)$$

where $\sigma_1(t)$, $\sigma_2(t)$, $\sigma_3(t)$ represent the stress with the applied frequency of 45 kHz, 80 kHz, and 100 kHz respectively. A_0 represents the stress amplitude at a frequency of 45 kHz. f_1, f_2, f_3 represent frequencies of 45 kHz, 80 kHz, and 100 kHz, respectively.

The stress distribution on the $BaTiO_3$ single crystals is provided in Fig. S10 (ESI†). The relationship between the output voltage of the piezoelectric potential and the applied stress is as follows:[12,51,52]

$$D = d\sigma + \varepsilon E \quad (10)$$

$$V = \frac{DH}{\varepsilon} \quad (11)$$

where D is the electric displacement, d is the piezoelectric coefficient, ε is permittivity, E is external electric field which is approximately equal to 0 here, and H represents thickness of piezoelectric materials. Therefore, the higher the applied external force, the higher the electric displacement and the higher the piezoelectric potential obtained, which is consistent with the results in Fig. 3.

The exchange–correlation effect of DFT was represented by the generalized gradient approximation (GGA) in the form of Revised Perdew–Burke–Ernzerhof (RPBE) functional and OTFG ultrasoft pseudo-potentials were employed for the core electrons. A plane-wave cut-off energy of 489.8 eV was used in the calculations. A four-layer model of $BaTiO_3$ with (001) and (110) surfaces was established. The bottom two layers were fully fixed, while the remaining two layers' atoms were in a fully relaxed state. A vacuum layer of 15 Å was created along the *Z*-axis to prevent periodic interactions. The termination surfaces of $BaTiO_3$ with (001) and (110) surfaces and the selection of hydrogen adsorption sites were determined based on the principle of lowest energy.[53]

The calculation of hydrogen adsorption free energy is performed using the following formula:

$$\Delta G_{H^*} = \Delta E + \Delta ZPE - T\Delta S + \Delta G(pH) \quad (12)$$

where ΔE, ΔZPE, T, ΔS, and $\Delta G(pH)$ represent the binding energy, difference in zero-point energy, temperature, entropy change, and pH correction term, respectively.

ΔE is calculated from the energies of the slab with H*, pure slab, and hydrogen gas:

$$\Delta E = E(\text{slab with } H^*) - E(\text{pure slab}) - \frac{1}{2}E(H_2) \quad (13)$$

Zero-point energy refers to the lowest possible energy that a quantum mechanical physical system may have. The zero-point energy of the pure surface can be neglected,[54] ΔZPE was calculated by

$$\Delta ZPE = E_{ZPE}^{H} - E_{ZPE}^{H_2} \quad (14)$$

As the phonon mode changes of the adsorbed H* on the surface can be neglected, the entropy change can be corrected as follows:

$$\Delta S = -\frac{1}{2}S_{H_2}^0 \quad (15)$$

The pH correction term was calculated by ref. 38

$$\Delta G(pH) = -kT \times \ln(10 \times pH) \quad (16)$$

k is the Boltzmann constant, and pH value of 7 was chosen in this work as the deionized water was employed.

Author contributions

Y. Z., D. Z. and J. R. initiated this work. J. R. supervised the method of mechanical imprint. F. Z. carried out deformation experiments and prepared the samples. F. N. collected the optical images. M. S. and S. X. performed the TEM experiments. K. F., Y. Z., Y. Z, H. G and T. F. conducted the electrochemical measurements and analyzed the data. K. F. performed the piezoelectric catalysis experiments. K. F., Y. Z., F. Z. and T. F. provided insights into the piezoelectric catalysis mechanism. K. F. carried out the DFT calculations. F. D. performed the NMR measurements with the guidance and analysis of G. B. Y. Z., K. F., M. S. and F. Z. wrote the first manuscript with contributions from all authors. J. R. and C. B. reviewed the final version of the manuscript. All authors contributed to data analysis and commented on the manuscript.

Data availability

The data that support the findings of this study are available from the corresponding author upon reasonable request.

Conflicts of interest

The authors declare no competing interests.

Acknowledgements

Y. Z. acknowledges support from the National Key Research and Development Program (2022YFB3807404), the National Natural Science Foundation of China (no. 52302158), Xiaomi Young Talents Program and Humboldt Research Fellowship for Experienced Researchers (Dr Yan Zhang). J. R. acknowledges funding from the German Research Foundation (DFG) under project no. 414179371. F. Z. acknowledges support from the Alexander von Humboldt Foundation for the fellowship with award number 1203828 and the DFG through project no. 530438323. G. B. acknowledges funding from the DFG under contract Bu-911-28-2. C. B. acknowledges support of UKRI Frontier Research Guarantee on "Processing of Smart Porous Electro-Ceramic Transducers – ProSPECT", Project No. EP/X023265/1. We thank Professor K. Durst for access to the LEXT laser scanning microscope. We appreciate Phadcalc (**https://www.phadcalc.com**) for the excellent TEM service.

References

1 F. Perera and K. Nadeau, *N. Engl. J. Med.*, 2022, **386**, 2303–2314.
2 X. Y. Tian, P. C. Zhao and W. C. Sheng, *Adv. Mater.*, 2019, **31**, 1808066.
3 H. F. Qiu, T. Yang, J. Zhou, K. Yang, Y. R. Ying, K. D. Ding, M. Yang and H. T. Huang, *J. Mater. Chem. A*, 2023, **11**, 7034–7042.
4 M. van der Spek, C. Banet, C. Bauer, P. Gabrielli, W. Goldthorpe, M. Mazzotti, S. T. Munkejord, N. A. Rokke, N. Shah, N. Sunny, D. Sutter, J. M. Trusler and M. Gazzani, *Energy Environ. Sci.*, 2022, **15**, 1034–1077.
5 L. H. Lin, W. Ren, C. Wang, A. M. Asiri, J. Zhang and X. C. Wang, *Appl. Catal., B*, 2018, **231**, 234–241.
6 Y. Zheng, Y. Jiao, A. Vasileff and S. Z. Qiao, *Angew. Chem., Int. Ed.*, 2018, **57**, 7568–7579.
7 C. B. Bie, L. X. Wang and J. G. Yu, *Chem*, 2022, **8**, 1567–1574.
8 V. R. Stamenkovic, D. Strmcnik, P. P. Lopes and N. M. Markovic, *Nat. Mater.*, 2017, **16**, 57–69.
9 S. C. Tu, Y. X. Guo, Y. H. Zhang, C. Hu, T. R. Zhang, T. O. Y. Ma and H. W. Huang, *Adv. Funct. Mater.*, 2020, **30**, 2005158.
10 M. B. Starr and X. D. Wang, *Sci. Rep.*, 2013, **3**, 2160.

11 M. B. Starr, J. Shi and X. D. Wang, *Angew. Chem., Int. Ed.*, 2012, **51**, 5962–5966.
12 H. Y. Gong, Y. Zhang, J. J. Ye, X. Zhou, X. F. Zhou, Y. Zhao, K. Y. Feng, H. Luo, D. Zhang and C. Bowen, *Adv. Funct. Mater.*, 2024, **34**, 2311091.
13 K. Wang, C. Han, J. Q. Li, J. S. Qiu, J. Sunarso and S. M. Liu, *Angew. Chem., Int. Ed.*, 2022, **61**, e202110429.
14 N. Meng, W. Liu, R. Y. Jiang, Y. Zhang, S. Dunn, J. Y. Wu and H. X. Yan, *Prog. Mater. Sci.*, 2023, **138**, 101161.
15 C. F. Gorin, E. S. Beh and M. W. Kanan, *J. Am. Chem. Soc.*, 2012, **134**, 186–189.
16 C. F. Gorin, E. S. Beh, Q. M. Bui, G. R. Dick and M. W. Kanan, *J. Am. Chem. Soc.*, 2013, **135**, 11257–11265.
17 E. S. Beh, S. A. Basun, X. F. Feng, I. U. Idehenre, D. R. Evans and M. W. Kanan, *Chem. Sci.*, 2017, **8**, 2790–2794.
18 A. Kakekhani and S. Ismail-Beigi, *J. Mater. Chem. A*, 2016, **4**, 5235–5246.
19 S. Kumar, M. Sharma, T. Frömling and R. Vaish, *J. Ind. Eng. Chem.*, 2021, **97**, 95–110.
20 C. Y. Wang, C. Hu, F. Chen, T. Y. Ma, Y. H. Zhang and H. W. Huang, *Nano Energy*, 2023, **107**, 108093.
21 X. F. Zhou, S. H. Wu, C. B. Li, F. Yan, H. R. Bai, B. Shen, H. R. Zeng and J. W. Zhai, *Nano Energy*, 2019, **66**, 104127.
22 G. D. Yang, Q. Chen, W. J. Wang, S. J. Wu, B. J. Gao, Y. B. Xu, Z. Chen, S. X. Zhong, J. R. Chen and S. Bai, *ACS Appl. Mater. Interfaces*, 2021, **13**, 15305–15314.
23 Y. W. Feng, L. L. Ling, Y. X. Wang, Z. M. Xu, F. L. Cao, H. X. Li and Z. F. Bian, *Nano Energy*, 2017, **40**, 481–486.
24 H. Li, C. Tsai, A. L. Koh, L. L. Cai, A. W. Contryman, A. H. Fragapane, J. H. Zhao, H. S. Han, H. C. Manoharan, F. Abild-Pedersen, J. K. Norskov and X. L. Zheng, *Nat. Mater.*, 2016, **15**, 48.
25 W. Dong, H. Y. Xiao, Y. M. Jia, L. Chen, H. F. Geng, S. U. Bakhtiar, Q. Y. Fu and Y. P. Guo, *Adv. Sci.*, 2022, **9**, 2105368.
26 S. Kumar, M. Sharma, A. Kumar, S. Powar and R. Vaish, *J. Ind. Eng. Chem.*, 2019, **77**, 355–364.
27 M. Höfling, L. Porz, M. Scherer, S. Gao, F. P. Zhuo, D. Isaia and J. Rödel, *J. Mater. Res.*, 2022, **37**, 737–746.
28 M. Höfling, X. D. Zhou, L. M. Riemer, E. Bruder, B. Z. Liu, L. Zhou, P. B. Groszewicz, F. P. Zhuo, B. X. Xu, K. Durst, X. L. Tan, D. Damjanovic, J. Koruza and J. Rödel, *Science*, 2021, **372**, 961.
29 F. Zhuo, X. Zhou, S. Gao, M. Höfling, F. Dietrich, P. B. Groszewicz, L. Fulanović, P. Breckner, A. Wohninsland, B.-X. Xu, H.-J. Kleebe, X. Tan, J. Koruza, D. Damjanovic and J. Rödel, *Nat. Commun.*, 2022, **13**, 6676.
30 Y. Oshima, A. Nakamura and K. Matsunaga, *Science*, 2018, **360**, 772–774.
31 Q. K. Muhammad, L. Porz, A. Nakamura, K. Matsunaga, M. Rohnke, J. Janek, J. Rödel and T. Frömling, *Nano Energy*, 2021, **85**, 105944.
32 E. Navickas, Y. Chen, Q. Y. Lu, W. Wallisch, T. M. Huber, J. Bernardi, M. Stöger-Pollach, G. Friedbacher, H. Hutter, B. Yildiz and J. Fleig, *ACS Nano*, 2017, **11**, 11475–11487.
33 C. Rodenbücher, S. Menzel, D. Wrana, T. Gensch, C. Korte, F. Krok and K. Szot, *Sci. Rep.*, 2019, **9**, 2502.
34 Q. K. Muhammad, M. Scherer, A. K. Opitz, S. Taibl, C. Boehme, M. Rohnke, J. Janek, S. Gao, J. Fleig and T. Frömling, *ACS Nano*, 2022, **16**, 16655–16667.
35 M. Kissel, L. Porz, T. Frömling, A. Nakamura, J. Rödel and M. Alexe, *Adv. Mater.*, 2022, **34**, 2203032.
36 S. H. Wang, L. L. Wang, L. B. Xie, W. W. Zhao, X. Liu, Z. C. Zhuang, Y. L. Zhuang, J. Chen, S. J. Liu and Q. Zhao, *Nano Res.*, 2022, **15**, 4996–5003.
37 F. Zhuo, X. Zhou, F. Dietrich, M. Soleimany, P. Breckner, P. B. Groszewicz, B.-X. Xu, G. Buntkowsky and J. Rödel, *Adv. Sci.*, 2024, 2403550.
38 S. L. Liu, Z. Hu, Y. Z. Wu, J. F. Zhang, Y. Zhang, B. H. Cui, C. Liu, S. Hu, N. Q. Zhao, X. P. Han, A. Y. Cao, Y. N. Chen, Y. D. Deng and W. B. Hu, *Adv. Mater.*, 2020, **32**, 2006034.
39 V. Faka, M. T. Agne, M. A. Lange, D. Daisenberger, B. Wankmiller, S. Schwarzmuller, H. Huppertz, O. Maus, B. Helm, T. Boger, J. Hartel, J. M. Gerdes, J. J. Molaison, G. Kieslich, M. R. Hansen and W. G. Zeier, *J. Am. Chem. Soc.*, 2024, **146**, 1710–1721.
40 Q. Liu, Q. Hu, D. Zhai, Q. W. Sun, H. Luo and D. Zhang, *J. Mater. Chem. A*, 2021, **9**, 17841–17854.
41 Y. Wang, Y. Xu, S. Dong, P. Wang, W. Chen, Z. Lu, D. Ye, B. Pan, D. Wu, C. D. Vecitis and G. Gao, *Nat. Commun.*, 2021, **12**, 3508.
42 Q. Liu, D. Zhai, Z. Xiao, C. Tang, Q. Sun, C. R. Bowen, H. Luo and D. Zhang, *Nano Energy*, 2022, **92**, 106702.
43 C. Tsai, H. Li, S. Park, J. Park, H. S. Han, J. K. Norskov, X. L. Zheng and F. Abild-Pedersen, *Nat. Commun.*, 2017, **8**, 15113.
44 G. Maciejewski, S. Kret and P. Ruterana, *J. Microsc.*, 2006, **223**, 212–215.
45 D. Cherns, C. G. Rao, H. Mokhtari, J. Cai and F. A. Ponce, *Phys. Status Solidi B*, 2002, **234**, 924–930.
46 M. Y. Yan, S. W. Liu, Z. D. Xiao, X. Yuan, D. Zhai, K. C. Zhou, D. Zhang, G. D. Zhang, C. Bowen and Y. Zhang, *Ceram. Int.*, 2022, **48**, 5017–5025.
47 W. Amdouni, M. Fricaudet, M. Otoničar, V. Garcia, S. Fusil, J. Kreisel, H. Maghraoui-Meherzi and B. Dkhil, *Adv. Mater.*, 2023, **35**, 2301841.
48 F. P. Zhuo, X. D. Zhou, S. Gao, F. Dietrich, P. B. Groszewicz, L. Fulanovi, P. Breckner, B. X. Xu, H. J. Kleebe, D. Damjanovic and J. Rödel, *Phys. Rev. Lett.*, 2023, **131**, 016801.
49 J. Zheng, Y. Guo, L. Zhu, H. Deng and Y. Shang, *Ultrasonics*, 2021, **115**, 106456.
50 S. Merouani, O. Hamdaoui, Y. Rezgui and M. Guemini, *Ultrason. Sonochem.*, 2013, **20**, 815–819.
51 J. Zhang, S. Ye, H. Liu, X. Chen, X. Chen, B. Li, W. Tang, Q. Meng, P. Ding, H. Tian, X. Li, Y. Zhang, P. Xu and J. Shao, *Nano Energy*, 2020, **77**, 105300.
52 X. Liu, J. Liu, L. He, Y. Shang and C. Zhang, *Adv. Funct. Mater.*, 2022, **32**, 2201274.
53 P. Abbasi, M. R. Barone, M. D. Cruz-Jáuregui, D. Valdespino-Padilla, H. Paik, T. Kim, L. Kornblum, D. G. Schlom, T. A. Pascal and D. P. Fenning, *Nano Lett.*, 2022, **22**, 4276–4284.
54 Y. M. Fo and X. Zhou, *Int. J. Hydrogen Energy*, 2022, **47**, 19073–19085.

